DOI: 10.13009/EUCASS2017-242



# Investigation on Recess Variation of a Shear Coaxial Injector in a GOX-GCH4 Rectangular Combustion Chamber with Optical Access

*Simona Silvestri*, Fernanda Winter*, Mattia Garulli**, Maria Palma Celano*, Gregor Schlieben*, Oskar Haidn* and Oliver Knab****

** Institute of Turbomachinery and Flight Propulsion (LTF), Technische Universität München (TUM)*
*Boltzmannstraße 15, 85748 Garching b. München, Germany*
***Politecnico di Torino*
*Corso Duca degli Abruzzi 24, 10129 Torino, Italy*
****Airbus Safran Launchers GmbH*
*Robert-Koch-Strasse 1, 82024 Taufkirchen, Germany*

## Abstract

In the current study the effects of oxidizer post recess length variation in a shear coaxial injector have been experimentally investigated. Different injector configurations are used to inject oxygen and methane, both in gaseous form, into the combustion chamber at representative rocket engine conditions. The combustion chamber is of a square cross-section and it is equipped with optical access. The results reveal that the recess changes the flame shape and the heat release distribution in the near injector field. In addition, the pressure drop across the injector, the heat flux distribution and the combustion efficiency all assume higher values for all the recess lengths tested than the flush mounted case

## 1. Introduction

Hydrocarbon propellants are attractive in the space propulsion field due to their ease in handling and low operational costs. In particular, oxygen/methane is one of the most promising hydrocarbon propellant combinations since it features high specific impulse, low coking tendency and good performance. The design and optimization of liquid rocket engines using methane require a detailed knowledge and understanding of the dominating physical phenomena of propellant injection, combustion and heat transfer. Although studies have already been performed [1, 2, 3], the current knowledge in oxygen/methane combustion, flame stabilization and injector design criteria is missing a wide-ranging experimental and analytical database. Because the combustor performance of liquid rocket engines is strongly influenced by the injection process, the injector design is very crucial in the rocket engine development.

In the context of the national research program Transregio SFB/TRR-40 on “Technological Foundations for the Design of Thermally and Mechanically Highly Loaded Components of Future Space Transportation Systems”, combustion and heat transfer of rocket combustion chambers operated with gaseous oxygen (GOX) and gaseous methane (GCH4) for different injector configurations are experimentally and numerically investigated.

A round and a rectangular single element chamber are built and tested. The injector element used for both the hardware is a shear coaxial type and allows the variation of several recess lengths. In previous studies [4, 5] the round combustion chamber has been tested with recess lengths that varied from *3 mm* to *12 mm*. comparing detailed analysis of the experimental results of all different recess length cases revealed that the GOX post recess enhances the mixing of the propellants when its length was longer than one GOX post exit diameter. The longer the recess length, the higher was the influence on the injector pressure drop and on the heat loads to the wall in the near injector region. Furthermore, it has been discovered that only the *12 mm* recess length configuration had a substantial improvement in combustion performance. To better understand the effect of recess length on the flame behaviour the injector has been mounted in a rectangular combustion chamber equipped with optical access, having similar geometric and performance characteristic of the round chamber [6]. In this paper the influence of the recess on the combustion heat release profile as well as on the combustion efficiency is investigated at *20 bar* combustion chamber pressure and for several mixture ratios. Classical measurement techniques together with optical diagnostic methods

DOI: 10.13009/EUCASS2017-242



are used to reconstruct the temperature field in the chamber wall material and determine the flame behaviour in the near injector region.

## 2. Test specimen and experimental configuration

All experiments have been performed at the Institute of Flight Propulsion's mobile test facility at the Technical University of Munich (TUM). The movable test bench allows experiments with gaseous methane and gaseous oxygen for combustion chamber pressures up to *20 bar*. In this section a brief description of the single element rocket combustion chamber, the injector geometry, the measurement equipment and data analysis procedures is presented.

### 2.1 Hardware description

The presented test campaign is performed using a modular single element heat-sink combustion chamber made of oxygen-free copper (Cu-HCP) designed for a testing time of up to *4 s* at a chamber pressure of 20 *bar*. The combustion chamber, depicted in Figure 1 is of square cross-section with an inner dimension of *12 mm* and a length of *290 mm*. A brass structure holds on the top wall a quartz glass window, allowing an optical access of *40 mm* by *12 mm*. The window internal face is cooled by gaseous nitrogen film. The mass flow rate of nitrogen is negligible and does not perturb the main flow. The nozzle differs from a usual configuration due to its throat with a rectangular cross section of *4.8 mm x 12 mm*, which results in a contraction ratio of 2.5 and Mach number in the chamber of 0.24. The ignition is achieved by a torch igniter using gaseous methane/gaseous oxygen, mounted in the middle of the combustion chamber.

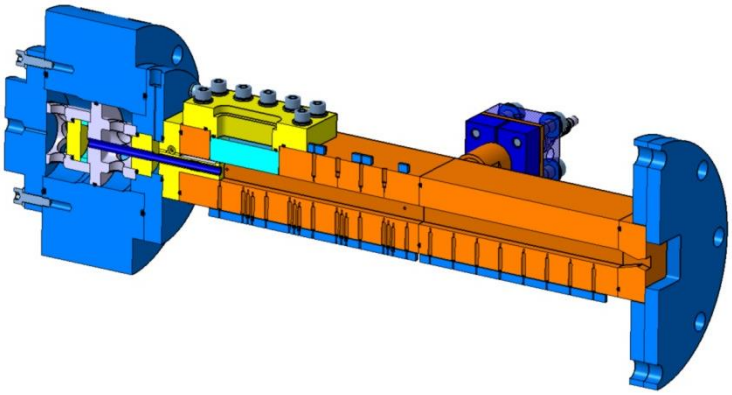

Figure 1. Combustion chamber schematic

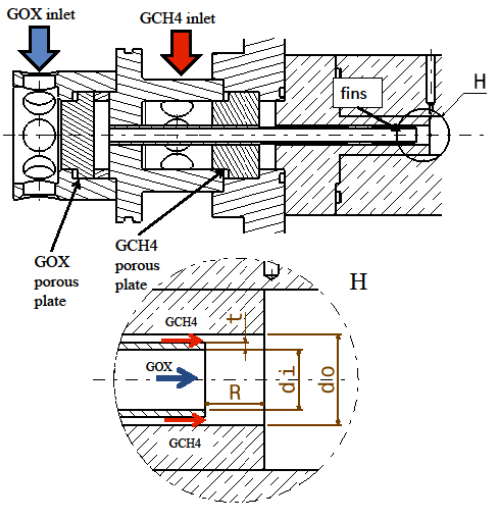


Figure 2. Schematic of the injector

Table 1. Injector dimensions

| | | | |
|---|---|---|---|
| GOX inner diameter | $d_i$ | [mm] | 4 |
| GCH4 outer diameter | $d_o$ | [mm] | 6 |
| GOX post wall thickness | $t$ | [mm] | 0.5 |
| GOX post length | $l$ | [mm] | 96 |
| GOX post recess | *R0* | [mm] | 0 |
| GOX post recess | *R9* | [mm] | 9 |
| GOX post recess | *R12* | [mm] | 12 |
| GOX post recess | *R15* | [mm] | 15 |
| Taper angle | | [°] | 0 |
| Injector area ratio | $A_{GCH4}/A_{GOX}$ | [-] | 0.7 |

DOI: 10.13009/EUCASS2017-242



The injector head of the combustor is designed to allow different injector configurations. For the current study, four variants of the single shear coaxial injector element are used. A flush mounted configuration and three recess lengths, defined as the axial distance R separating the GOX tube exhaust and the injection plane, of *9 mm* (R9), *12 mm* (R12) and *15 mm* (R15) are chosen. Those lengths correspond respectively to 2.25 x, 3 x, and 3.75 x $d_i$. Recess variation is achieved by adding cylindrical disks of different length between the faceplate segment and the oxygen manifold. Table 1 shows the main characteristic dimensions of the injectors. The injector element is centered in the faceplate by four equally-spaced fins. For the current test series, the fins are positioned with an angle of 45° to the combustion chamber center plane. To ensure homogeneous injection conditions, in terms of temperature, pressure and velocity and to reduce the influence of the upstream feed lines, two porous plates are placed in the oxidizer and fuel manifolds. A schematic of the injector design for the recessed configuration is shown in Figure 2.

## 2.2 Experimental setup

The hardware is equipped with standard instrumentations required to characterize the operation of the chamber. For a better understanding of the complex heat transport processes, equally spaced pressure transducers on the side wall provide for a well resolved measurement path of the wall pressure distribution *p(z)* along the chamber axis. WIKA A10 pressure transducers are used to record the axial evolution of the static chamber wall pressure. The pressure sensors are individually calibrated and operated at a data acquisition rate of *100 Hz*. To characterize the injection conditions, thermocouples of type K, with *0.5 mm* diameter, and pressure transducers are installed in the chamber manifolds, prior the porous plates. A schematic of the combustion chamber and the associated sensor locations is given in Figure 1. To determine the temperature field within the chamber material, thermocouples are embedded at a series of evenly distributed axial positions on the bottom wall of the chamber. Type T thermocouples of *0.5 mm* diameter are located within the chamber wall with *1 mm* distance from the hot gas side. The thermocouples are kept in position by a spring loaded system. This spring loading provides a constant force of about *2 N*, which ensures a continuous contact between the thermocouple tip and the base of the hole. This setup aims to minimize the chance of potential loss of contact as the material undergoes expansion and contraction due to changes in temperature or vibrations during the hot run [7]. More details about the experimental set-up can be found in previous publications [8].
Additionally to the classical measurements setup a monochromatic camera (BU205M with CMOS image sensor) equipped with a doubled spectral filter combination (Schott UG11 and Schott WG305) is used to detect spontaneous OH emission. The flame emission is collected at a frame rate of 168 Hz with an optical resolution of 2048×1088 pixels. To cover the full dynamic range of the system, the exposure time has been fixed at *50 µs* when the filter was not used and *5000 µs* when the filter was applied. More information about the optical setup can be found in Winter et al. [9].

## 2.3 Operating conditions

In the present experiments, the chamber pressure is limited to nominal *20 bar*. Mixture ratios that vary from 2.2 to 3.4 have been tested. Figure 3 and Figure 4 give an overview of the actual conditions, mass flow rate and mean combustion chamber pressure, obtained during the test campaign. Each operating point is run at least two times to check the repeatability of the recorded test data for a burning time of *3 s*. Each operating point and its repetition are presented in the following paragraphs. From the figures it can be seen that the combustion chamber pressure obtained in the recessed cases, achieved with the same mass flow rate conditions, is higher than those in the flushed mounted case. Since the performance of a rocket is positively correlated with the chamber pressure, it can be expected, as shown in Section 3.6 that the recess of GOX post improves the performance of the engine.

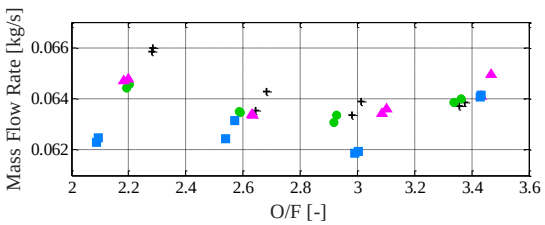


Figure 3. Operated test conditions

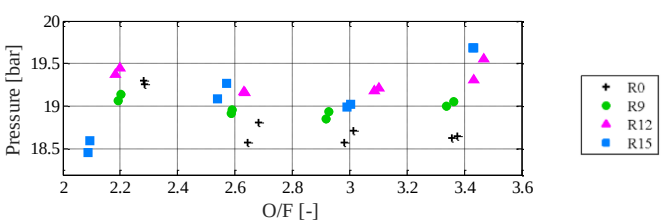


Figure 4. Mean combustion chamber pressure

DOI: 10.13009/EUCASS2017-242



# 3. Experimental results

## 3.1 Near-injector flame shape and jet-dynamics

The single jet-flame formed by the coaxial injector fed by gaseous oxygen in the inner tube and gaseous methane in the external annulus is analysed by imaging the light emitted by hydroxyl (OH) radicals. Rotational symmetry of the flame is not exactly verified because the flow is confined by a chamber with a square cross-section. It is expected however that the distortion associated with the corner vortices will remain small and the perturbation of the boundary flow conditions in case of a flat window in a round chamber cross-section would have a bigger impact.
Considering the results obtained by taking averages of instantaneous emission images corresponding to the operating points at mixture ratio of 2.2 and 3.4, Figure 5 gives the measured emission distribution for the four injector configurations. The injector external geometry is shown on the left of each figure. The flow direction is from left to right. The averaging was carried out over 50 images with, each image having an exposure time of *5000 µs*. From the top to the bottom each injector configuration with increasing recess lengths is shown. On the left, the load point with mixture ratio equals to 2.2, on the right the mixture ratio equals to 3.4 are displayed. It is clearly visible that the recess modifies the region of OH emission in a substantial way. The images indicate that the total flame emission right after injection is stronger with recess. That can be related to a better mixing of the propellants. The total flame volume within the optical accessible area appears to be larger in case of a recess is applied. This effect is visible on all the mixture ratios tested and in conformance with LOX/H2 investigations performed by Kendrick et al. [10] and with LOX/CH4 investigations performed by Lux et al. [11] on coaxial injectors.
Shear coaxial injector flow fields are generally confined with the central oxygen jet persisting well into the combustion chamber [12, 13]. In case of the flush mounted configuration, the flame is initially cylindrical and envelops the GOX jet. The flame then progressively moves away from the central axis and the emission zone becomes thicker. The flame continues to expand until the end of the visible optical access, where starts to assume again a cylindrical shape. In case the GOX tube is recessed, the flame is thicker near the injector plane; it expands rapidly and assumes a conical shape. At a greater distance the flame appears again like a thick quasi-cylindrical shell. For both operating points the flame zone expands faster and occupies a larger volume of the chamber. With increase recess length, a larger expansion angle is visible. Although the flame shape appears different for each injector configuration studied, the emission region features a maximum size at about 4.9 x $d_i$ from the injector plane for all the recess lengths tested. Beyond this section, the diameter of the flame diminishes slowly with distance and assumes a cylindrical shape. Even though it is not possible to deduce the local exact emission values from an observation under a single viewing angle, an average light intensity is calculated processing the imaging emissions on MATLAB. The light intensities obtained are not meant to be considered in absolute value; however a comparison between the emissions in the different cases can be performed. The corresponding results for the cases analysed in Figure 5 are given in Table 2. A deviation of ±2% has to be taken into account due to the lower light intensity in the zone where a crack appears on the window surface or when soot deposition is present. As can be seen from Figure 5 a crack on the window surface is visible almost at the end of the optical access for the R0 configuration tests and in the near injector position for the R12 configuration tests. The test with the R9 and R15 configurations show instead a thin soot layer in the near injector region.

Table 2. Time and axial averaged OH emission intensity

| | Injector configuration | | | |
|---|---|---|---|---|
| | R0 | R9 | R12 | R15 |
| OF=2.2 | 77.5 | 102.4 | 134.4 | 158.1 |
| OF=3.4 | 69.0 | 97.1 | 139.5 | 161.5 |

To characterize the strong dynamic of the propellant jet that enters the combustion chamber, the variance of the flame contour is calculated over 50 images, each image has been exposed over a period of *50µs*. In fact, although averaged images only provide an insight into the mean flame shape, the single shots offer a high temporal resolution. Figure 6 shows the variance of the flame contour for the OF=2.2 case on the left and OF=3.4 case on the right for all the injector configurations tested. While for the reference case the fluctuations of the flame appear to be concentrated in the second part of the optical access, increasing the recess length, the fluctuations move forward and become closer to the injector plane. Furthermore, it has been found that for the lower mixture ratio case, where the external methane jet is faster than the internal oxygen jet, the fluctuations appear more concentrated on the external boundary layer and the flame appears thicker. For the higher mixture ratio case, where the internal oxygen jet is predominant, the flame assumes a thinner shape, transported downstream from the oxygen jet. Here fluctuations are mainly visible in the shear layer between the propellants.

DOI: 10.13009/EUCASS2017-242



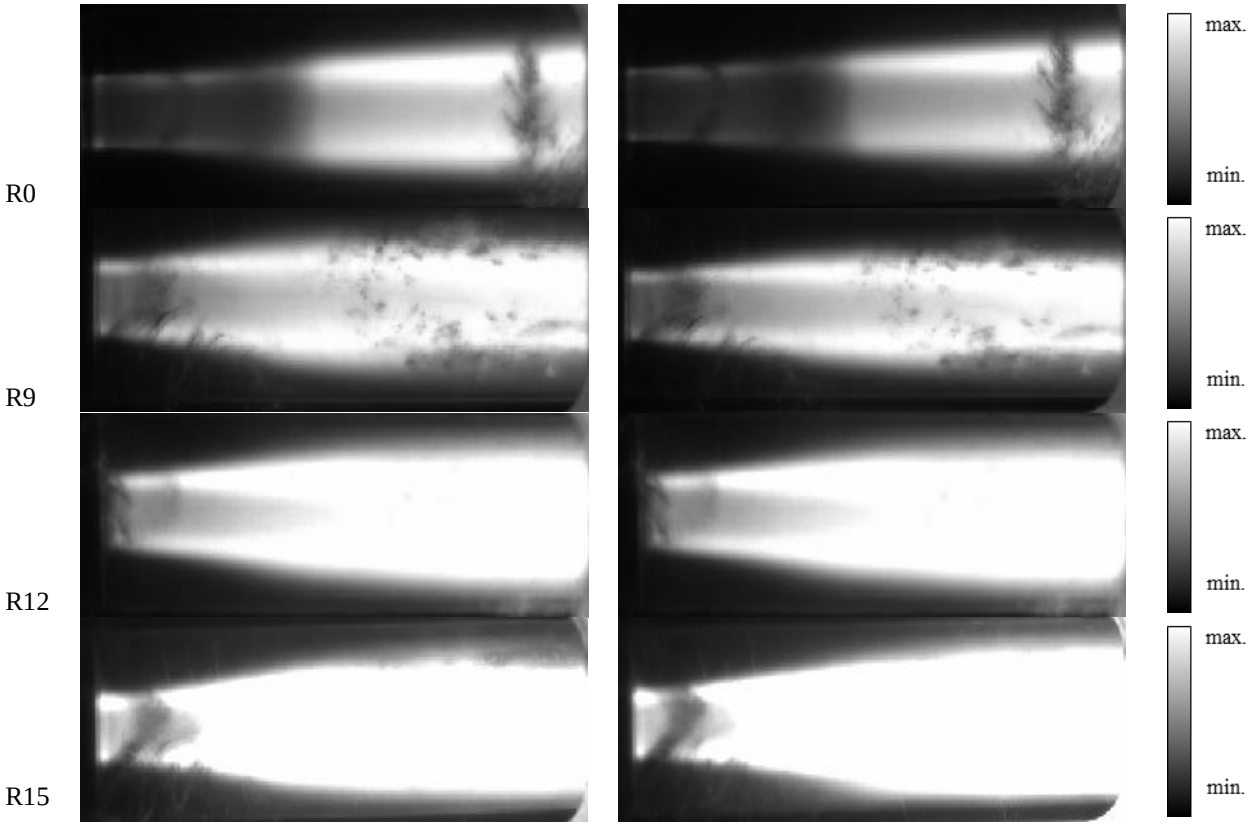


Figure 5. Averaged OH emission (40 x 12 mm$^2$), exposure time 5000 µs, OF=2.2 on the left and OF=3.4 on the right.

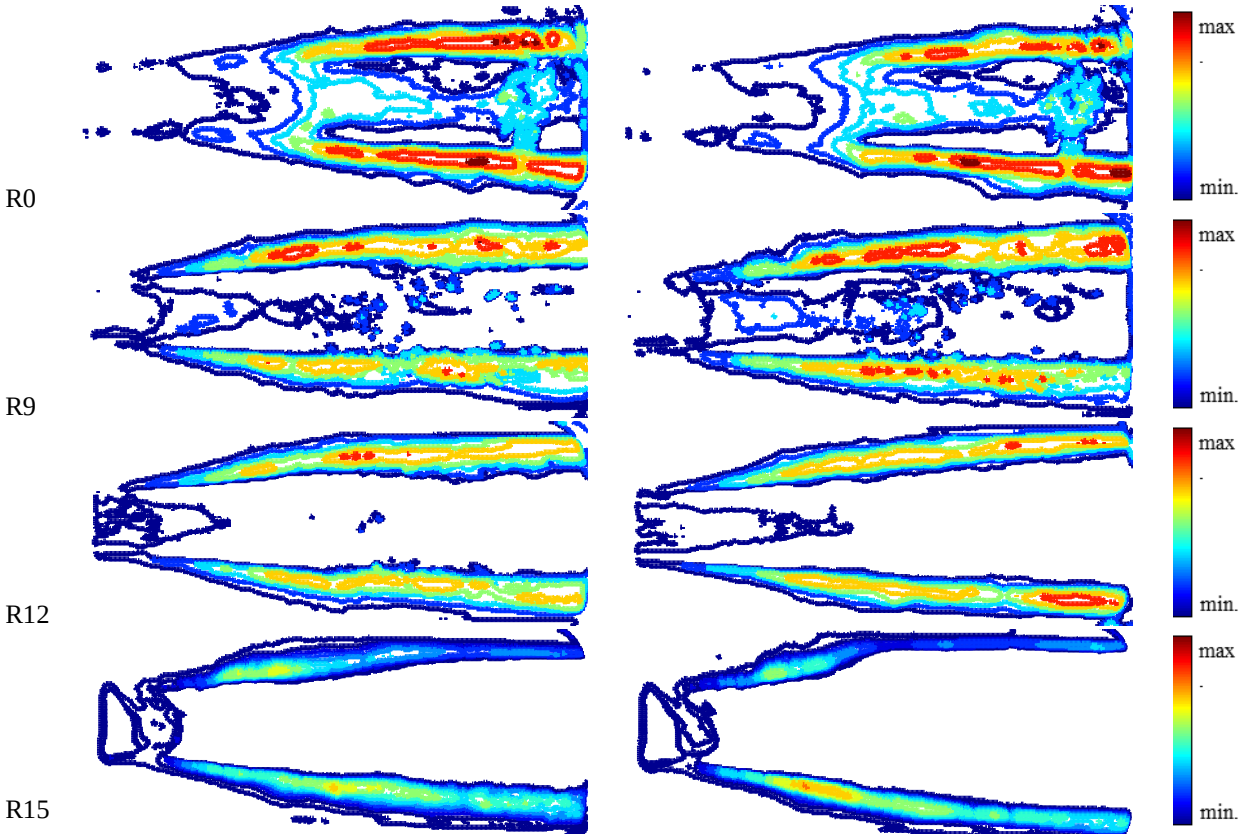


Figure 6. Variance of the near-injector jet (40 x 12 mm$^2$), exp. time 50 µs, of n=50 consecutive images.

DOI: 10.13009/EUCASS2017-242



### 3.2 Injector pressure drop

In standard cryogenic flames, a jet of low velocity oxidizer is surrounded by an annulus of co-flowing fuel at high velocity. The annulus flow continually sheds the liquid core into ligaments and drops, till only the droplet field remains. When the LOX tube is recessed inside the fuel tube, the combustion products will both block and add heat to the fuel flow. The presence of the flame inside the duct and the associated flow of hot products will accelerate the gaseous stream; consequently an additional pressure loss within the injector will be produced. One of the big differences between fluids at sub-critical and super-critical pressures bases on their thermodynamic properties. At super-critical pressure, surface tension and liquid/gas phase changes diminish. As a result the oxygen in the combustion chamber no longer experiences liquid atomization, but rather diffuses directly through turbulent mixing similar to a turbulent gas jet [5]. Thus, the effects of recess on a liquid/gas coaxial jet do not necessarily correspond to those on a coaxial jet at super-critical pressures. Therefore no substantial variation in the injector pressure drop is expected.
Two coefficients $K_M$ and $K_O$ are defined to describe the increase in pressure drop at the injector. To correct the dependency of the pressure drop to different injection conditions, the actual mass flow rate is taken as normalization factor. The maximum increase in friction, incrementing with the length of the recess from 0 mm to 15 mm is negligible compared to the results obtained.

$$K_M = \frac{\left(\frac{\Delta P_{CH4}}{\dot{m}^2_{CH4}}\right)_{Recess} - \left(\frac{\Delta P_{CH4}}{\dot{m}^2_{CH4}}\right)_{R0}}{\left(\frac{\Delta P_{CH4}}{\dot{m}^2_{CH4}}\right)_{R0}} \tag{1}$$

$$K_O = \frac{\left(\frac{\Delta P_{GOX}}{\dot{m}^2_{GOX}}\right)_{Recess} - \left(\frac{\Delta P_{GOX}}{\dot{m}^2_{GOX}}\right)_{R0}}{\left(\frac{\Delta P_{GOX}}{\dot{m}^2_{GOX}}\right)_{R0}} \tag{2}$$

Figure 7 and Figure 8 show the variation of $K_M$ and $K_O$ as a function of the mixture ratio. The increase in pressure drop is expected to be higher for the methane side, due to the lower density, which provides less resistance towards the expanding flame than the much denser oxygen. This effect becomes more pronounced at higher mixture ratios, where the amount of methane is minimized. Furthermore, the higher is the oxygen mass flow rate; the higher is the suction effect on the methane side. This effect tends to be compensated by the internal blocking produced by the flame. Although, a general intensification of the pressure drop is observable when the recess length increases, the flow needs a certain length to interact. For the R9 recess configuration the effects of internal suction and expansion of the flame compensate and only a low influence is visible for the variation of mixture ratio. For the longer recess lengths the expansion capability of the flame that enters the chamber is sufficiently high to have a significant influence. In this case a strong variation of *KM* and *KO* is visible with the variation of mixture ratio. For the R15 configuration an increase of about 30% is noticeable.

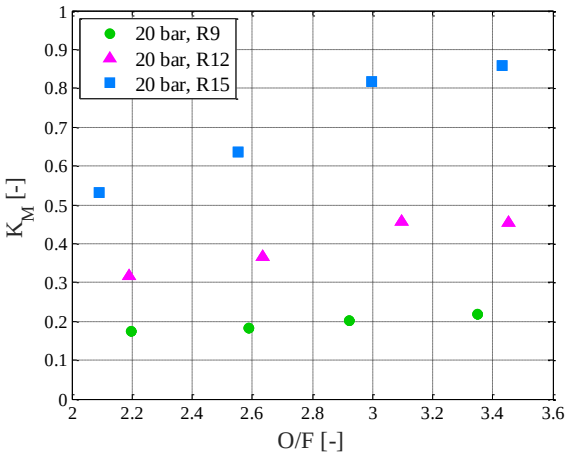


Figure 7. KM, methane coefficient

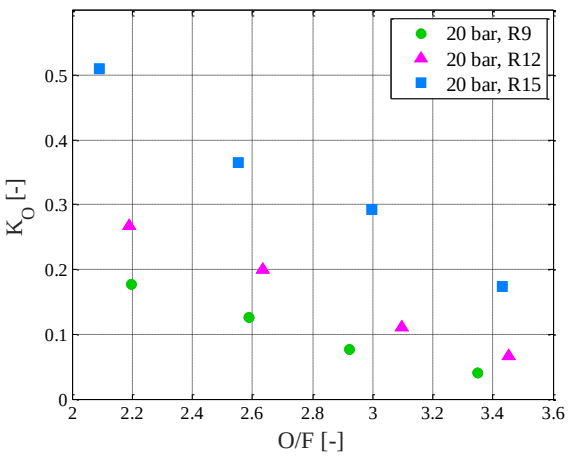


Figure 8. KO, oxygen coefficient

DOI: 10.13009/EUCASS2017-242



### 3.3 Temperature distribution

Due to the transient nature of the hardware, a proper time window needs to be chosen for the evaluation of the test data. To check the influence of the start-up and shut-down phase, the burning time is divided in six sectors, each of them of *0.5* s duration. The difference of the temperature readings due to heat up in each time sector is calculated for the OF=3.4 for the configurations studied. The thermocouples, placed at *1 mm* distance from the hot gas side, along the combustion chamber axis, are used for the evaluation. Figure 9 shows the difference in temperature for the first four time sectors. Initially, the thermal energy produced by the ignition and the interference of the igniter stream with the main flow have a strong impact on the temperature gradient, nevertheless after *0.5* s the influence is almost negligible and the temperature signals shown rise smoothly. The energy produced by the igniter is absorbed by the copper wall and produces a non-homogenous temperature field in the material. The conduction of the heat through the copper walls needs a certain time to dissipate the initial temperature inhomogeneity. Figure 10 displays the axial temperature level at each time interval for the case mentioned. It can be seen that the time required to dissipate the initial temperature discrepancy exceeds the whole burning time. The initial foot print on the material tends to flatten but remains visible. A similar behavior has been encountered also at Penn State Laboratory and at Beijing University. Although in previous publications [14, 15], the reason was not well understood, the bumping profile is characteristic of capacitive hardware and the peaks become more pronounced for small injector-wall distances.
To allow good comparability of the evaluated data points, the effect of the transient start-up and shut-down in the temperature readings has to be isolated. For this reason the temperature distribution along the combustion chamber axis is assumed as a temperature difference between the signal at *2/3* of the burning time (evaluation time) and an initial time of *0.5* s after ignition.

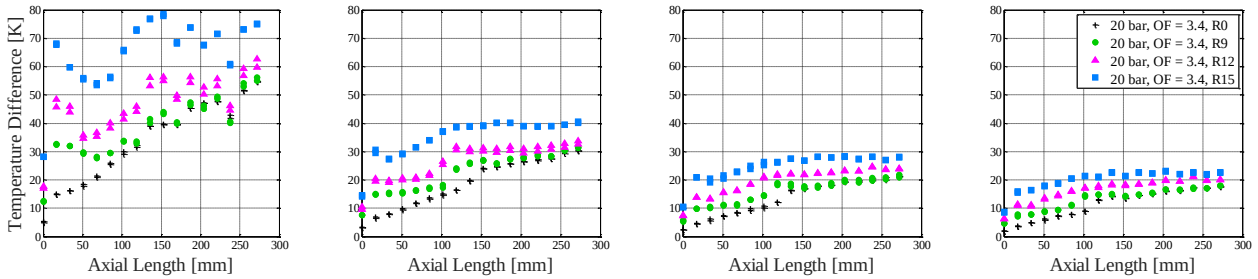


(a) Δt=(0.5-0) s (b) Δt=(1-0.5) s (c) Δt=(1.5-1) s (d) Δt=(2-1.5) s

Figure 9. Temperature difference along the chamber axis at each 0.5 s time interval

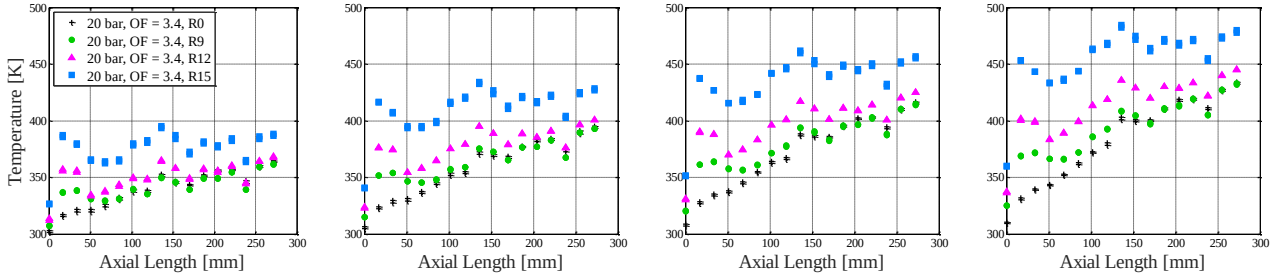


(a) t=0.5 s (b) t=1 s (c) t=1.5 s (d) t=2 s

Figure 10. Temperature value along the chamber axis each 0.5 s

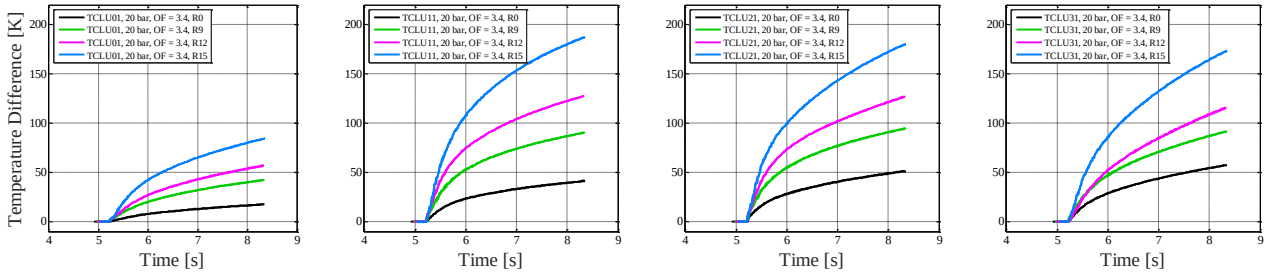


(a) z=0.5 mm (b) z=17.5 mm (c) z=34.5 mm (d) z=51.5 mm

Figure 11. Normalized temperature signal over burning time

DOI: 10.13009/EUCASS2017-242



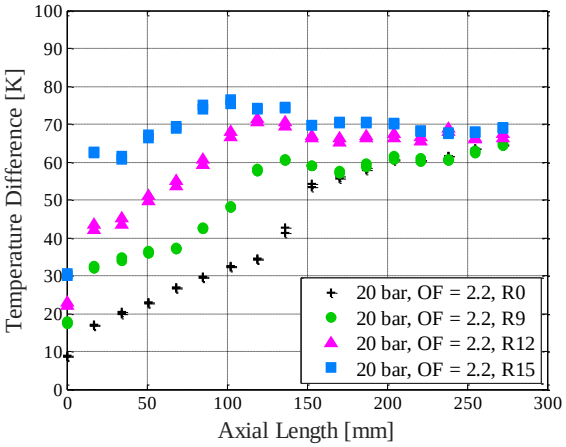


Figure 12. Temperature difference at evaluation time, OF=.2.2

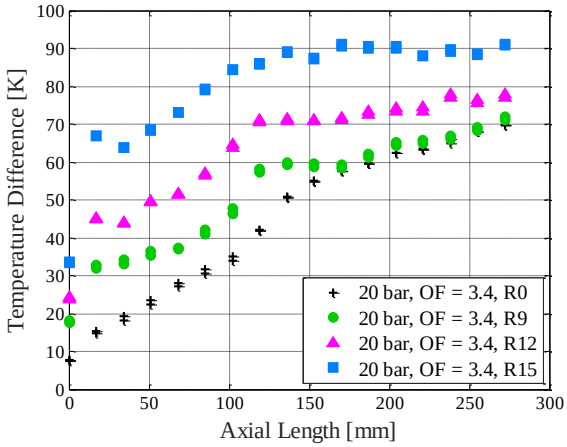


Figure 13. Temperature difference at evaluation time, OF=3.4

The temperature distribution for the different injector configurations and mixture ratios equal to 2.2 and 3.4 are shown in Figure 12 and Figure 13, respectively. In the first half of the chamber, the temperature increases gradually with increasing the recess length for both the mixture ratios. In the second half of the chamber, the overall level of the temperature difference remains roughly constant for OF=2.2. For OF=3.4 an increase in the temperature level is visible for the longer recess configurations. Moreover, a different steepness of the temperature profile is noticeable for each configuration studied. While for the reference configuration the temperature increases continuously along the chamber axis, with increasing recess length the temperature profile becomes flatter starting from a higher initial value at the injection plane. For the *15 mm* recess length a temperature increase of almost 40% is recognizable at the injector plane and the flattening of temperature profile starts *75 mm* away from the faceplate.
To better analyze the physical mechanisms in the near-injection region, the signal of the first four thermocouples, normalized for the initial temperature, is reported in Figure 11 for the different injector configurations at OF=3.4. The signals, zoomed into the hot firing part, display a substantial rise of the slope with increasing the recess length. In transient conditions, the energy absorbed by the combustion chamber wall is proportional to the energy released by the combustion processes. Hence for a given time interval, higher heat release would lead to higher temperature gradients in the structure. This can be related to a better initial mixing in the near injector region. Moreover, at the stagnation point, where the flame impacts the wall, the boundary layer is more disturbed and a more intensive flame would produce a higher temperature level of the wall. This is confirmed by the maximum variation in the temperature gradient seen for the second thermocouple position, placed at z = 17 mm. This effect can be directly correlated to a bigger expansion angle of the jet and a stronger flame emission as already shown in Section 3.1.

### 3.4 Heat flux distribution

For the calculation of the heat flux based on the thermocouple measurements, an inverse computational method has been developed [16, 17]. The applied tool relies on an iterative method, which aims to minimize the residual function. In this case, the residual function is defined as the difference between measured and calculated temperature values. To achieve that, the code takes advantage of the conjugate gradient method to optimize the unknown boundary condition at the hot gas chamber wall. The optimization is carried out for each time step separately. Starting from an initial guess for the heat flux, a direct problem is solved which means that the heat flux PDEs are solved leading to the temperature field in the whole chamber for the present time step. The temperature difference between calculated and measured temperature at all thermocouple locations is used by the conjugate gradient optimization algorithm to update the applied boundary heat flux. After a sufficient number of iteration the residual becomes small enough so that convergence is achieved and the next time step is calculated. Upon convergence of the final time step, a complete time dependent profile for the heat flux and the temperature is obtained for all the points in the domain. The solution of the direct problem is done with a Finite Difference code which solves the discretized energy equation in the 3D domain of the combustion chamber. The resulting heat flux is determined solely by the thermocouple measurements placed in the down part of the chamber and the conduction properties of the chamber. The computational domain is simplified and restricted to the combustion chamber, starting from the faceplate and ending at the axial position where the nozzle begins. The nozzle itself is not included, since no sensors are attached in this engine segment and therefore, no information about its temperature can be obtained. The discontinuity of material caused by the presence of the quartz window on the top surface of the chamber is neglected. The small

DOI: 10.13009/EUCASS2017-242



dimension of the window compared to the overall domain and its distance to the thermocouples, minimize the influence of an adiabatic surface on the average heat flux distribution. The differences obtained are minimal and are considered acceptable for the present work and comparison.
A correction of the heat flux that takes into account variations in injection conditions which could slightly vary for each test (see Figure 3) is necessary for a better comparison of the cases under study. Heat transfer correlations available in literature [18] indicate that the heat transfer coefficient is proportional to the pressure to the power of 0.8. To decouple the contribution to the chamber pressure produced by different mixing efficiency, a correction that takes into account the partial and total mass flow rates injected is applied as in Eq. (3).

$$\dot{q}_{nom} = \dot{q}_{test}\left[\frac{(\dot{m}c^*_{th})_{nom}}{(\dot{m}c^*_{th})_{test}}\right]^{0.8} \tag{3}$$

The results obtained for the *20 bar* case, at OF=2.2 and OF=3.4, are taken as example of the test results and are shown respectively in Figure 14 and Figure 15. As can be seen the peaks in the temperature profile, discussed in section 3.3, are still visible in the heat flux profile, since the optimization used is based on the temperature values.
Due to steady combustion, the heat flux increases continuously along the chamber axis till the accomplishment of the reaction process. Shear coaxial injector flow fields are generally confined with the central oxygen jet persisting well into the chamber and consequently, it is not surprising that for the R0 configuration the maximum level of wall heat flux is close to the combustion chamber end. When a recess is applied the maximum heat flux level is moved upstream and a starting higher level of heat flux is visible close to the injector. In the first half of the chamber, for the R9 and R12 cases, the heat flux is independent on the mixture ratio tested, as effect of the enhancement mixing produced by the recess, the heat flux level increases with recess length. Moreover, the heat flux profiles grow parallel along the chamber axis and assume a more convex shape compared to the R0 case. In the second half of the chamber, for OF=2.2, the heat flux profiles is flatter, while the R9 configuration tends to achieve the same level of the R0 case of circa *5 MW/m²*, a slightly higher level of *5.5 MW/m²* is achieved by the R12 configuration. For OF=3.4, the heat flux profile still grows parallel along the chamber axis and the heat flux level continuously increases until the end of the combustion chamber. Also in this case the R9 configuration tends to assume the same value of the R0 case of circa *6 MW/m²* and a slight increase of *0.5 MW/m²* is visible for the R12 configuration. In the near injector region, the dominating factor is the initial mixing of the propellants. The heat loads are determined by the growth rate of the boundary layer and the amount of propellant burnt. Therefore, the quantity of oxygen in the system, hence the variation of mixture ratio, does not affect the heat flux profile. Proceeding towards the nozzle, the dominating phenomenon for the heat release becomes the combustion itself. Hence, a growth of the heat flux level is expected for higher mixture ratios.
Different behavior is shown by the R15 configuration, which not only produces a substantial increase in the heat flux, but also a different characteristic of the profile. The major part of the combustion process appears to be finished in the first half of the chamber and the heat flux profile assumes almost a flat shape. While for OF=2.2 the heat flux profile decreases after *z=150 mm* from the injector assuming a value of *6 MW/m²*, for OF=3.4 the profile slowly increases reaching a value of circa *8 MW/m²*.

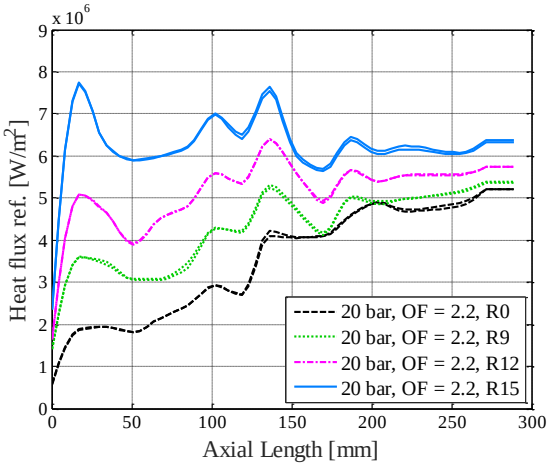

Figure 14. heat flux axial distribution, OF=2.2

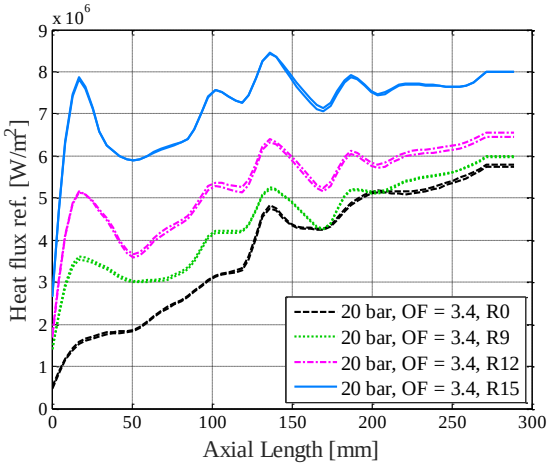

Figure 15. Heat flux axial distribution, OF=3.4

DOI: 10.13009/EUCASS2017-242



To better quantify the effect of the recess on total heat loss through the chamber wall the integrated heat flux can be determined. The values are summarized in the Table below. The surface occupied from the quartz window has been considered as adiabatic.

Table 3. Integrated heat flux.

| Injector configuration | Units | OF=2.2 | OF=3.4 |
|---|---|---|---|
| R0 | [kW] | 47.2 | 49.7 |
| R9 | [kW] | 54.8 | 57.6 |
| R12 | [kW] | 65.2 | 68.3 |
| R15 | [kW] | 74.7 | 91.4 |

### 3.5 Pressure distribution

The design of the combustion chamber allows for the implementation of a high number of pressure sensors equally spaced with a distance twice the spacing for the temperature measurements. Due to the combustion process the mixture injected will accelerate from injection velocity up to hot gas velocity. Consequently, the wall pressure is expected to decrease along the chamber axis, according to Bernoulli's equation. An indicator of completeness of the combustion process is the flattening of the pressure gradient. As example of the test results obtained for the different injector configurations, the OF=2.2 and OF=3.4 test cases are presented in Figure 16 and Figure 17, respectively. The wall pressure distribution for all the configurations tested is normalized with the reading of the last pressure sensor in the chamber, mounted shortly upstream the throat at *z=272 mm*. In the region close to the faceplate is observable a drop in wall pressure, linked to the presence of a recirculation zone. No variations of the stagnation point are observed for the configurations studied.

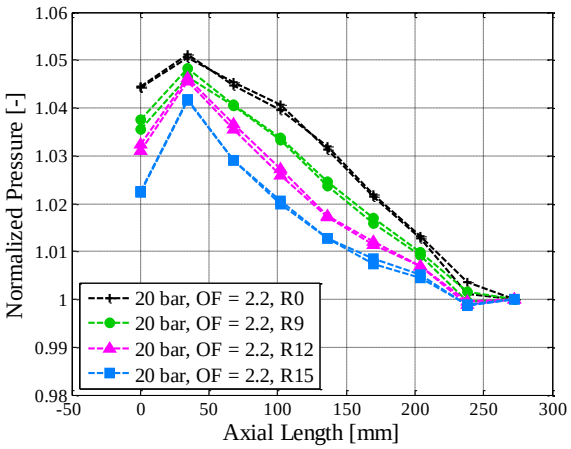


Figure 16. Normalized pressure distribution, OF=2.2

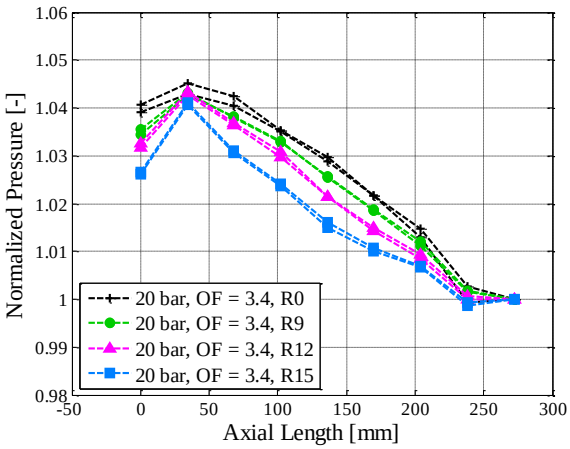


Figure 17. Normalized pressure distribution, OF=3.4

A lower pressure decay level ($\Delta p/\Delta z$) along the combustion chamber axis, encountered for the recess cases, is an indicator for a better mixing between methane and oxygen flows. Indeed, lower pressure decay corresponds to lower axial acceleration of the combusted gas in the chamber. In fact the gases, already accelerated in the recess region, are injected with a higher velocity into the chamber and the required acceleration to match the combustion velocity diminishes. For the OF=2.2 case, a lower pressure decay is visible increasing the recess length, 1% difference in pressure decay is achieved by the R15 configuration. Instead, for the OF=3.4 case, the pressure decay is almost negligible. In general a pressure gradient of up to 4% of the combustion chamber pressure is visible for all the configurations studied. Although a flattening of the pressure profile is visible only at the end of the combustion chamber, a remarkable variation in the profile shape can be noticed in all the mixture ratios studied. While for the R0 configuration the pressure profile appears to have a concave shape, when the recess length increases, the shape changes its concavity until it assumes a convex shape for the R15 configuration.
As already analyzed in Silvestri et al. [19], the results show that the use of recess improves the initial mixing between the propellants. This improvement is mostly local and affects the region close to the injector. Only after a certain length, in the cases tested 3 x $d_i$, this enhancement influences the global combustion process. This effect appears to

DOI: 10.13009/EUCASS2017-242



have more influence for lower mixture ratios, where the amount of oxygen burnt inside the recess length is higher and the shear forces obtainable with this injector design are maximized.

### 3.6 Performance parameters

The combustion efficiency [20] in a liquid rocket engine is typically defined as in Eq. (4):

$$\eta_{c^*} = \frac{c^*_{exp}}{c^*_{theo}} \tag{4}$$

where $c^*_{exp}$ is the actual value of the characteristic velocity determined from the experiment and $c^*_{theo}$ is the theoretical ideal characteristic velocity determined here using NASA's CEA code. Two different efficiencies are determined from the experiment [19]. An overall thrust chamber $\eta^{TC}_{c^*}$ efficiency and an injector related energy release efficiency $\eta^{ER}_{c^*}$, in which the energy leaving the combustor through the walls is taken into account for the calculation of the theoretical characteristic velocity. Figure 18 and Figure 19 show the combustion efficiency for the injector configurations studied as a function of the mixture ratio.

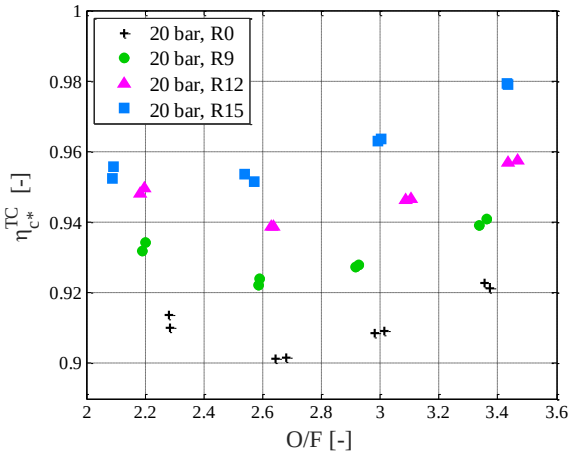


Figure 18. Thrust chamber efficiency.

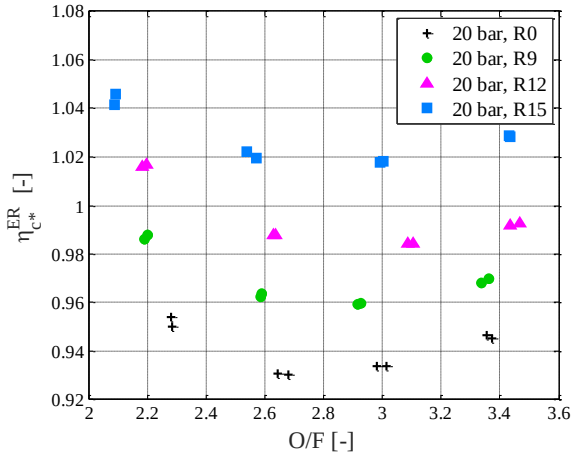


Figure 19. Energy release efficiency.

As can be seen the effect of the heat loss on the combustion efficiency, when taken into account, is quite substantial. For the R15 case the combustion efficiency is over 100 percent, which theoretically is not possible. A probable reason for this behavior is the neglection of other effects that could potentially increase the theoretically achievable characteristic velocity, such as chemical kinetic effects, two-dimensional flow features or boundary layer effects. A considerable improvement in combustion efficiency is obtained for all the configurations studied. The longer the recess, the higher is the combustion efficiency obtained. An improvement of circa 2%, 4% and 6% is achieved by the R9, R12 and R15 configuration.

The combustion efficiency increases as a result of improved mixing of the propellants; however the pressure drop throughout the injector increases as well. To distinguish the effectiveness of the mixing obtained compared to the pressure losses at the injector, an injector based efficiency needs to be determined. On this purpose, two coefficients are introduced. The coefficients $G_M$ and $G_O$ are defined as in Eq. (6) and Eq. (7):

$$G_M = \frac{(Pc)_{Recess} - (Pc)_{R0}}{\Delta p_{inj,CH4}} \tag{5}$$

$$G_O = \frac{(Pc)_{Recess} - (Pc)_{R0}}{\Delta p_{inj,O}} \tag{6}$$

They represent the gain in mean combustion chamber pressure to the losses in pressure drop at the methane and oxygen injector side. To better compare the improvement in combustion efficiency for the recess case, an efficiency factor ($K_{eta}$) is defined as in Eq. (7):

DOI: 10.13009/EUCASS2017-242



$$K_{eta} = \frac{(\eta_{c*})_{Recess} - (\eta_{c*})_{R0}}{(\eta_{c*})_{R0}} \tag{7}$$

Figure 20 and Figure 21 give the efficiency factor as function of the variation of the pressure drop on the oxygen and methane for the thrust chamber efficiency. The R0 configuration is taken as reference in the origin of the axis. The plot can be divided in four quadrants. Points belonging to the ($x>0$, $y>0$) quadrant have an improvement in the combustion efficiency, achieved without losses in combustion chamber pressure. The lower the pressure drop at the injector; the higher is the value of the abscissa. For the points belonging to the ($x<0$, $y>0$) quadrant, a better combustion efficiency is obtained although the mean pressure level is lower than the R0 case. For the point belonging to the ($x<0$, $y<0$) quadrant, no improvement in combustion efficiency has been encountered.
It has to be noticed that for each injector configuration studied the efficiency factor stays almost constant with variation of mixture ratios and increases with recess length. However for the OF=2.2 case, a high efficiency is obtained at the cost of increase pressure loss at the injector. The maximum gain is instead obtained for OF=3.4.

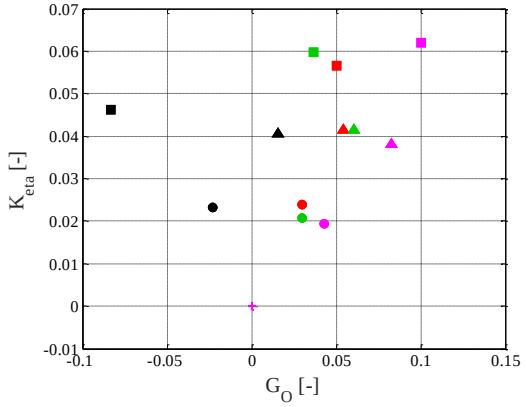


Figure 20. Efficiency factor oxygen.

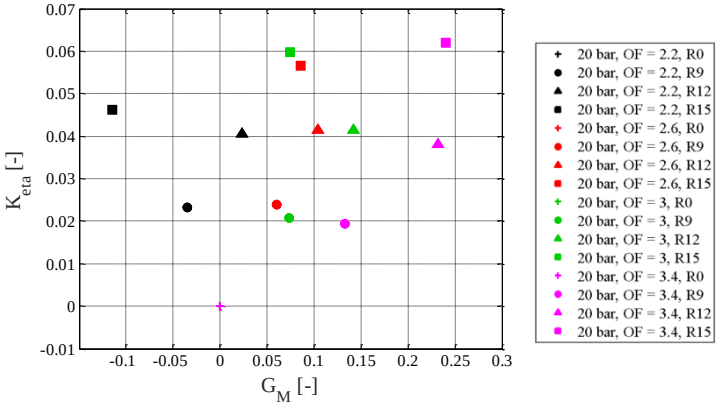


Figure 21. Efficiency factor methane.

## 4. Conclusion

The article deals with the effects of recess the oxygen tube of shear coaxial injector on heat load and combustion performance. The combustion chamber used is having a square internal cross section that allowed the installation of a quartz window in the near injector region. The experiments have been conducted for a wide range of mixture ratios at 20 bar combustion chamber pressure for recess lengths of *0 mm*, *9 mm*, *12 mm* and *15 mm*. The propellants used are gaseous oxygen and gaseous methane. High-speed OH emission images have been analyzed in details. It has been shown that a recessed GOX post modifies the region of OH emission in a significant way shortly after the injection. It has been proofed that the recess of the GOX tube changes the flame shape and the heat release distribution in the near field. The flame rapidly occupies a large volume, indicating that the mixing effects are faster when the GOX tube is recessed. The difference of mixture ratio variation in this zone appears to be negligible. The same effects have been seen in the axial load distribution. It has been found that the premixing area, provided by recessing the GOX post has a positive effect in the mixing and combustion characteristics of the shear coaxial injector. The longer the length of the recess, the higher is the heat flux and the combustion efficiency obtained. While in the near injector region this interaction appears to be independent by variation of the mixture ratio, a stronger effect is visible in the second half of the chamber.
To understand the effects in combustion performance of the different injector configurations, an injector based efficiency has been calculated. It has been discovered that the R15 injector configuration has a maximum improvement in combustion performance and that the mixture ratio variation plays a strong impact on the combustion mechanism. Additionally, the enhancement of the initial mixing affects both the near injection region and the main combustion process for all the recess configurations studied.

## 5. Acknowledgements

Financial support has been provided by German Research Foundation (Deutsche Forschungsgemeinschaft-DFG) in the framework of the Sonderforschungsbereich Transregio 40. The authors would like to thank Christian Bauer, Nikolaos Perakis and Christoph von Sethe for the support provided during the data analysis.

DOI: 10.13009/EUCASS2017-242



## References


[1] M. Burkhardt, M. Sippel, H. A. und K. J., „A propellant tradeoff for reusable liquid booster stages.," *Journal of Spacecraft and Rockets,* pp. 762-769, 2004.

[2] R. Schuff, M. Maier, O. Sindily, C. Ulrich und S. Fugger, „Integrated modelind and analisys for LOX/Methane expander cycle engine.," in *AIAA 2006-4534*, 2006.

[3] D. Preclik, G. Hagemann, O. Kanb, L. Brummer, C. Mäding und D. Wiedmann, „LOX/Hydrocarbon Propellant Trade Considerations for Future Reusable Liquid Booster Engines," in *AIAA Paper 2005-3567*, 2005.

[4] S. Silvestri, M. P. Celano, G. Schlieben, O. Knab und O. Haidn, „Experimental Investigation on Recess Variation of a Shear Coax Injector in a GOX-GCH4 Combustion Chamber," in *Space Propulsion*, Rome, 2016.

[5] S. Silvestri, M. P. Celano, C. Kirchberger, G. Schlieben, O. Haidn und O. Knab, „Investigation on Recess Variation of a Shear Coax Injector for a Single Element GOX-GCH4 Combustion Chamber," *Trans. JSASS Aerospace Tech. Japan,* Bd. 14, pp. 13-20, 2016.

[6] S. Silvestri, M. Celano, O. J. Haidn und O. Knab, „Comparison of Single Element Rocket Combustion Chambers with Round and Square Cross Sections," in *EUCASS*, 2015.

[7] D. Suslov, A. Woschnak, J. Sender und M. Oschwald, „Test Specimen Design and Measurement Technique for Investigation of Heat Transfer Processes in Cooling Channels of Rocket Engines Under Real Thermal Conditions.," in *AIAA 2003-4613*, 2003.

[8] M. Celano, S. Silvestri, G. Schlieben, C. Kirchberger, O. Haidn und O. Knab, „Injector Characterization for a GOX-GCH4 Single Element Combustion Chamber," *Progress in Propulsion Physics,* Nr. ISBN:978-5-94588-191-4, 2015.

[9] F. Winter, S. Silvestri, M. P. Celano und O. Haidn, „High Speed Imaging of a Coaxial Single Element GOX/GCH4 Rocket Combustion Chamber with Square Cross Section," in *7th EUCASS Conference*, Milan, 2017.

[10] D. Kendrick, G. Herding, P. Scouflaire, P. Scouflaire, J. C. Roolon und S. Candel, „Effects of a Recess on Cryogenic Flame Stabilization," *Combustion and Flame,* pp. 327-339, 1999.

[11] J. Lux, D. Suslov, M. Bechle, M. Oschwald und O. Haidn, „Investigation of sub-and supercritical LOX/Methane injection using optical diagnostics.," in *AIAA 2006-5077*, 2006.

[12] R. Woodward, S. Pal, S. Farhangi, G. Jensen und R. Santoro, „OX/GH2 Shear Coaxial Injector Atomization Studies: Effect of Recess and Non-Concentricity.," in *AIAA 2007-571*, 2007.

[13] R. D. Woodward, s. PAL, S. Farhangi und R. Santoro, „LOX/GH2 Shear Coaxial Injector Atomization Studies at Large Momentum Flux Ratios," in *42nd AIAA/ASME/ASEE Joint Propulsion Conference and Exhibit*, Sacramento, 2006.

[14] J. Locke, S. Pal und R. Woodward, „Chamber wall heat flux measuraments for a LOX/CH4 propellant uni-element rocket," in *AIAA 2007-5547*, 2007.

[15] G.-b. Cai, X.-w. Wang und T. Chen, „Method for Measurement of Single-Injector Heat transfer Characteristics and Its Application in Studying Gas-Gas Injector Combustion Chamber," in *Development in Heat Transfer*, Shanghai, Dr. Marco Aurelio Dos Santos Bernardes, 2011, pp. 455-476.

[16] M. P. Celano, S. Silvestri, J. Pauw, N. Perakis, F. Schily, D. Suslov und O. Haidn, „Heat flux evaluation methods for a single element heat-sink chamber.," in *6th European Conference for Aerospace Sciences*, 2015.

[17] N. Perakis, M. P. Celano und O. Haidn, „Heat flux and temperature evaluation in a rectangular multi-element GOX/GCH4 combustion chamber," in *7th EUCASS*, Milano, 2017.

[18] D. Bartz, „A simple equation for rapid estimation of rocket nozzle convective heat transfer coefficients.," *Journal of Jet Propulsion,* pp. 49-51, 1957.

[19] S. Silvestri, M. Celano, G. Schlieben, C. Kirchberger und O. Haidn, „Characterization of a GOX-GCH4 Single Element Combustion Chamber," in *Space Propulsion Conference*, 2014.

[20] G. Sutton, W. Wagner und S. J.D., „Advanced Cooling Techniques for Rocket Engines," *Astronautics and Aeronautics,* pp. 60-41, 1966.